Small-scale H I Channel Map Structure Is Cold: Evidence from Na I Absorption at High Galactic Latitudes

J. E. G. Peek[1,2] and S. E. Clark[3,4]

[1] Space Telescope Science Institute, 3700 San Martin Drive, Baltimore, MD 21218, USA
[2] Department of Physics & Astronomy, Johns Hopkins University, Baltimore, MD 21218, USA
[3] Institute for Advanced Study, 1 Einstein Drive, Princeton, NJ 08540, USA; seclark@ias.edu

Abstract

The spatial distribution of neutral hydrogen (H I) emission is a powerful probe of interstellar medium physics. The small-scale structure in H I channel maps is often assumed to probe the velocity field rather than real density structures. In this work we directly test this assumption, using high-resolution GALFA-H I observations and 50,985 quasar spectra from the Sloan Digital Sky Survey. We measure the equivalent widths of interstellar Na I D_1 and Na I D_2 absorption, and robustly conclude that together they depend nearly four times as strongly on the column density of small-scale structure in H I than on either the large-scale H I structure or the total H I column. This is inconsistent with the hypothesis that small-scale channel map structure is driven by velocity crowding. Instead, the data favor the interpretation that this emission structure predominantly originates in cold, dense interstellar material, consistent with a clumpy cold neutral medium.

1. Introduction

The diffuse interstellar medium (ISM) is sculpted by the interplay of many thermodynamic, magnetohydrodynamic, and chemical processes, and contains structure over a large range of scales. The morphology of diffuse gas and dust is an important diagnostic of the physics of the ISM. Small-scale structure in neutral hydrogen (H I) emission is of particular interest because it is preferentially aligned with the magnetic field, making the structure of H I a unique probe of the interstellar magnetic field (Clark et al. 2014, 2015; Martin et al. 2015; Kalberla et al. 2016; Blagrave et al. 2017; Clark 2018). Filamentary, magnetically aligned structures are also observed in other ISM probes, including H I absorption (McClure-Griffiths et al. 2006), dust emission (Planck Collaboration et al. 2016), and diffuse synchrotron emission (Jelić et al. 2015).

Interstellar H I is generically distributed into three phases, a warm neutral medium (WNM), cold neutral medium (CNM), and a thermally unstable medium (e.g., Cox 2005; Kalberla & Kerp 2009). While the linear H I self-absorption structures discovered by McClure-Griffiths et al. (2006) are unambiguously CNM, with spin temperatures of ~40 K, all three thermal phases can contribute to the observed H I emission. The magnetically aligned H I structures are most prominent in narrow channel maps: H I emission integrated over a few km s^{-1} in line velocity. The data thus far favor the interpretation that the magnetically aligned H I emission structures are preferentially CNM. Line width measurements of the H I ®bers are consistent with CNM temperatures (Clark et al. 2014; Kalberla et al. 2016).

Clark et al. (2019) went further, showing that the small-scale structure in H I channel maps *in general*—not just the prominently linear structure—is preferentially associated with cold-phase material. That work tested and ruled out a pervasive claim in the literature: that small-scale structure in H I channel map emission is dominantly or entirely "caustics" imprinted by the turbulent velocity field. The notion that H I channel map structure traces the velocity field leads to the incorrect conclusion that the magnetically aligned H I structures are neither CNM nor real density structures at all. This belief is summarized in Lazarian & Yuen (2018): "On the basis of Lazarian & Pogosyan (2000), one can conclude that the filaments observed by Clark et al. (2015) in thin channel maps can be identified with caustics caused by velocity crowding." Indeed, those authors' interpretation of Lazarian & Pogosyan (2000) is that in thin velocity channel maps "most of the structures should be due to velocity caustics." Instead, Clark et al. (2019) showed that (1) the H I channel map structures are correlated with broadband FIR emission, which is not sensitive to the velocity field; (2) that this correlation does not measurably decrease as the velocity channel width is decreased; and (3) that the FIR/$N_{\rm H I}$ ratio is preferentially higher toward smaller-scale channel map structures. None of these findings are consistent with measurable velocity caustics in H I.

Additionally, Clark et al. (2019) challenged the idea that the spatial power spectrum of narrow H I channel maps also can be used to measure the spectral index of the velocity power spectrum (see also Kalberla & Haud 2019). If narrow channel maps were structured by the velocity field, a shallower power spectrum would be measured for narrower channels (Lazarian & Pogosyan 2000). The converse of this argument holds that because narrower H I channels show shallower power spectra, the thin channel maps must be patterned by the velocity field. However, as Clark et al. (2019) point out, shallower power spectra in narrower channels are also qualitatively consistent with a higher fraction of the emission in narrow channel maps originating in CNM structures, which are smaller scale than the more diffuse WNM.

In this work, we carry out an independent test of the physical nature of this structure, using interstellar absorption lines in Sloan Digital Sky Survey (SDSS) quasar spectra. Specifically,

---

[4] Hubble Fellow.

we measure the behavior of the equivalent width (EW) of the Na I absorption line as a function of how much small-scale H I channel map $N_{\rm H\,I}$ the quasar sightlines traverse. Na I absorption is a direct tracer of cooler material in the ISM. The ratio $n_{\rm Na\,I}/n_{\rm H\,I}$ will increase in denser regions due to the $n_e \times n_{\rm ion}$ scaling of recombination and in cooler regions due to the $T^{-0.7}$ scaling of the radiative recombination coefficient (Hobbs 1975; Spitzer 1978; Draine 2011). If small-scale H I channel map structure is preferentially correlated with cold, dense regions of gas, then controlling for total H I column, the column of Na I and thus its EW will be higher for quasar sightlines that pass through more small-scale structure. If instead the small-scale H I channel map structure is "caustics caused by velocity crowding" (Lazarian & Yuen 2018), we would expect no increase in EW.

This Letter is organized as follows. In Section 2 we introduce the data products used. In Section 3 we detail our analysis of the correlation between small-scale H I channel map structure and Na I absorption measurements. In Section 4 we discuss how these results fit into a broader picture of ISM structure, and in Section 5 we conclude with implications of this work for statistical diagnostics of the turbulent ISM.

2. Data

2.1. GALFA-H I

We use archival 21 cm observations of the Milky Way ISM from GALFA-H I (Peek et al. 2018). These data, obtained with the 305 m Arecibo telescope in Puerto Rico, represent the highest angular (4′) and spectral (0.18 km s^{-1}) resolution large area (4 steradians, $-1° < \delta < 38°$) survey of the Galactic ISM to date. The data have been corrected for small angular scale sidelobe effects and spectral fixed pattern noise. We use the main $\delta v = 0.736$ km s^{-1} (Wide) data cubes as well as the total integrated H I intensity from -90 km s^{-1} < $v_{\rm LSR}$ < 90 km s^{-1}, which has been corrected for stray radiation. Stray radiation at Arecibo typically generates very large, smooth structures in H I maps, as the sidelobes are weak, distant, and broad. Since we are using the GALFA-H I data cubes only for small-scale structure, the lack of stray correction in these data is not an issue.

2.2. SDSS

We use archival spectroscopic observations of quasars from Sloan Digital Sky Survey Data Release 7 (SDSS DR7; Abazajian et al. 2009). These data have been used many times for spectroscopic absorption line studies of diffuse material, including of Na I D$_1$ and D$_2$ absorption in the Milky Way (Poznanski et al. 2012; Murga et al. 2015). Here we take advantage of the published continua as well, derived using nonnegative matrix factorization in Zhu et al. (2014). We access these data using the igmspec database published in Prochaska (2017). The entire database contains 105,783 quasars, with a wavelength resolution of $\lambda/\delta\lambda = 1800$.

3. Analysis

3.1. H I Structure

We construct a map of the small angular scale structure in the 21 cm data from GALFA-H I. To do this we first construct 27 channel maps of the 21 cm data with 3.68 km s^{-1} velocity width that span the velocity range

-48.21 km s^{-1} < $v_{\rm LSR}$ < 50.42 km s^{-1}. These maps cover the whole sky available in the data set. This velocity range includes nearly all Galactic emission and all significant small-scale structures at these latitudes; velocities beyond this range tend only to include noise and artifacts. We convert these maps to column densities under the assumption of optically thin H I, which is largely a good assumption at high Galactic latitude (Murray et al. 2018), where

$$N_{\rm H\,I} = 1.8 \times 10^{18}\ {\rm cm}^{-2} \frac{\int T_B dv}{\rm K\ km\ s^{-1}}. \qquad (1)$$

We then perform an unsharp mask on each of these maps. This procedure consists of smoothing the maps with a Gaussian of width FWHM $= 30′$, and subtracting the smooth map from the original data. This procedure is essentially equivalent to a Gaussian high-pass Fourier filter. We then threshold each of these maps, setting all values below 2×10^{18} cm^{-2} to zero, as a way to suppress artifacts caused by the observational scan pattern. We truncate the maps to the range $1° < \delta < 36°$ to reject some artifacts generated by the Arecibo ground screen (Peek et al. 2011), and we restrict the area to Galactic latitude $|b| > 30°$. We refer to this small-scale structure column density map as $N_{\rm H\,I}^{\rm SS}$ (see Figure 1). We perform the same δ and b cuts on the stray-corrected column density map, $N_{\rm H\,I}$, and define a large-scale structure column density map as

$$N_{\rm H\,I}^{\rm LS} = N_{\rm H\,I} - N_{\rm H\,I}^{\rm SS}. \qquad (2)$$

$N_{\rm H\,I}^{\rm LS}$ is "large-scale" in the sense that it is all of the H I column that is not in <30′ structures in the channel maps.

3.2. Quasar Spectra

We take the complete list of 105,783 quasars from SDSS DR7 and restrict to sources that are in the footprint described in Section 3.1, which gives us a final list of 50,985 quasar spectra. We interpolate these spectra, along with the paired continua from Zhu et al. (2014), onto a common wavelength grid from 5860 Å to 5940 Å in steps of 0.4 Å.

3.3. Stacking

Following Poznanski et al. (2012) and Murga et al. (2015), we perform median stacking of the continuum normalized, interpolated spectra. Median stacking has the strong advantage of rejecting outliers and the effects of incorrect telluric calibrations; indeed, we find mean stacking creates significantly noisier spectra. We find our results are qualitatively insensitive to choosing means or medians (see Section 4). We stack the quasar spectra in bins of the $N_{\rm H\,I}^{\rm SS}$ and $N_{\rm H\,I}^{\rm LS}$. We bin the data against $N_{\rm H\,I}^{\rm LS}$ in three bins (low, medium, and high), with the four bin edges equally spaced from 10^{20} cm^{-2} to 5×10^{20} cm^{-2}. We bin the data against $N_{\rm H\,I}^{\rm SS}$ in five bins. Four of these bins have bin edges evenly spaced from zero to 4×10^{19} cm^{-2}. We also include a fifth bin for $N_{\rm H\,I}^{\rm SS} = 0$, which has the largest number of sources. This creates a total of $3 \times 5 = 15$ bins. We select this binning to have sufficient Na I D$_1$ and Na I D$_2$ signal in each bin to make a reasonable measurement, while also including most (92%) of the sources. We note that perturbations to this binning do not qualitatively impact our results.
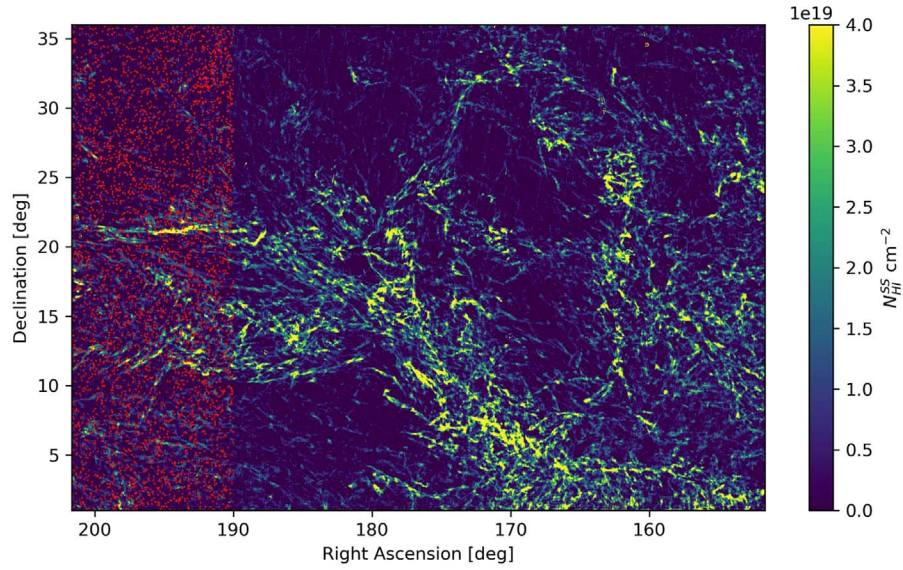
Figure 1. Section of the $N_{\mathrm{H\,I}}^{\mathrm{SS}}$ map at high Galactic latitude. The locations of quasars in our sample are shown in red for $l > 190°$, to give a sense of the density of the quasar sample on the sky without obscuring the rest of the map.

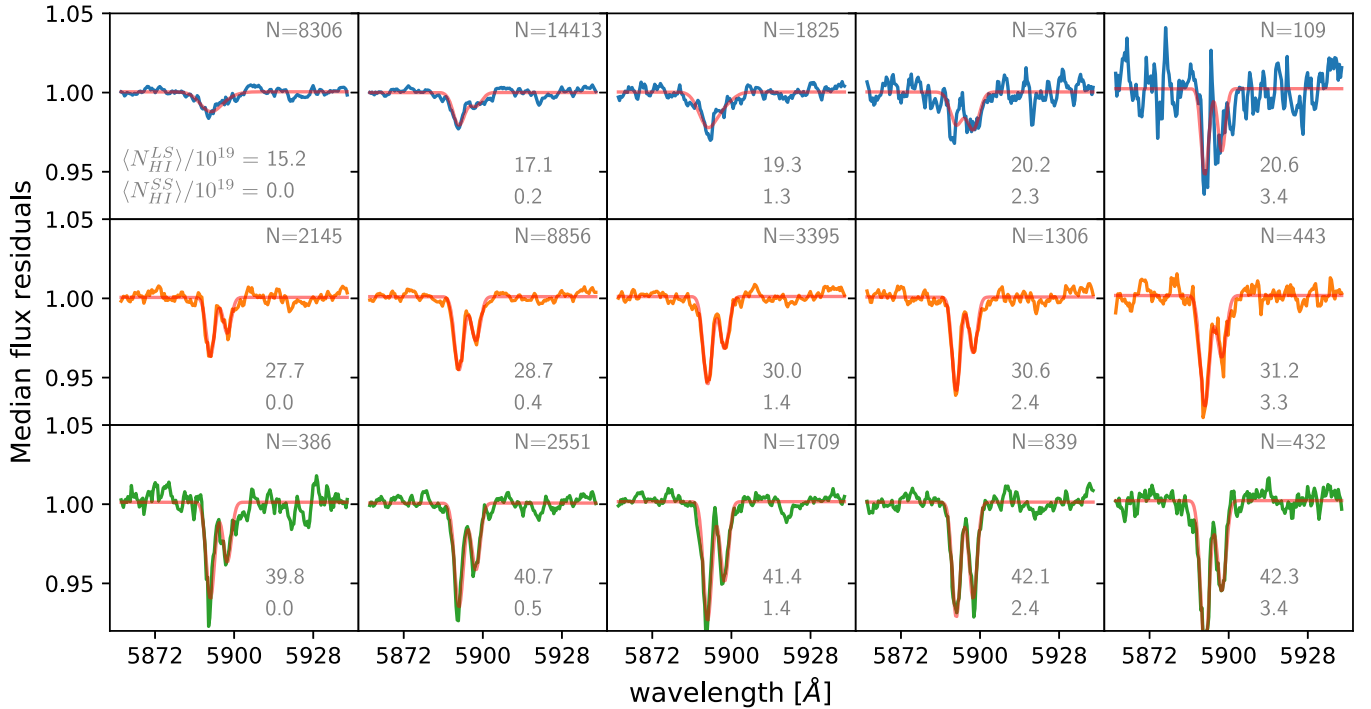**Figure 2.** Median stacks of Na I D_1 and D_2 absorption lines. Each panel is a median stack (blue, orange, or green) with a two-Gaussian fit overlaid (red). The leftmost column represents stacks where $N_{\mathrm{H\,I}}^{\mathrm{SS}} = 0$. The second through fifth columns represent stacks observed along lines of sight with $N_{\mathrm{H\,I},i} < N_{\mathrm{H\,I},U} \leqslant N_{\mathrm{H\,I},i+1}$, where $N_{\mathrm{H\,I},i} = [0, 1, 2, 3, 4] \times 10^{19}$ cm^{-2}. The jth row stacks spectra observed along lines of sight with $N_{\mathrm{H\,I},j} < N_{\mathrm{H\,I},S} \leqslant N_{\mathrm{H\,I},j+1}$, where $N_{\mathrm{H\,I},j} = [1, 2.33, 3.66, 5] \times 10^{20}$ cm^{-2}. The number of medianed spectra is marked in the upper right of each box, and the values of the median of the column densities are shown in the lower right, $\langle N_{\mathrm{H\,I}}^{\mathrm{LS}} \rangle$ (top) and $\langle N_{\mathrm{H\,I}}^{\mathrm{SS}} \rangle$ (bottom),

3.4. Fitting

We fit the Na I D_1 and Na I D_2 absorption lines in each of these median-binned spectra (Figure 2). We fit two Gaussians with independent amplitudes, but with wavelengths fixed to the rest frequency and only one width parameter used for both Na I D_1 and Na I D_2. We find the residual continua are generally quite well behaved in the medians, and fit only an additional overall offset parameter. We use the covariance between fit parameters to estimate the errors on the EWs on each line and

the system of both lines. In bins where both lines are robustly and clearly detected, the line ratio is between 1.6 and 1.35, indicating some saturation in the Na I D_2 line. In a completely optically thin regime the line ratio will asymptote to the ratio of the oscillator strengths, 2, and for the line ratios measured here we find opacities between 1 and a few (see, e.g., Draine 2011), though we note caution in interpreting these values physically, as they are measured in median stacks. We compile a measurement of the total EW of Na I D_1 and Na I D_2, shown in
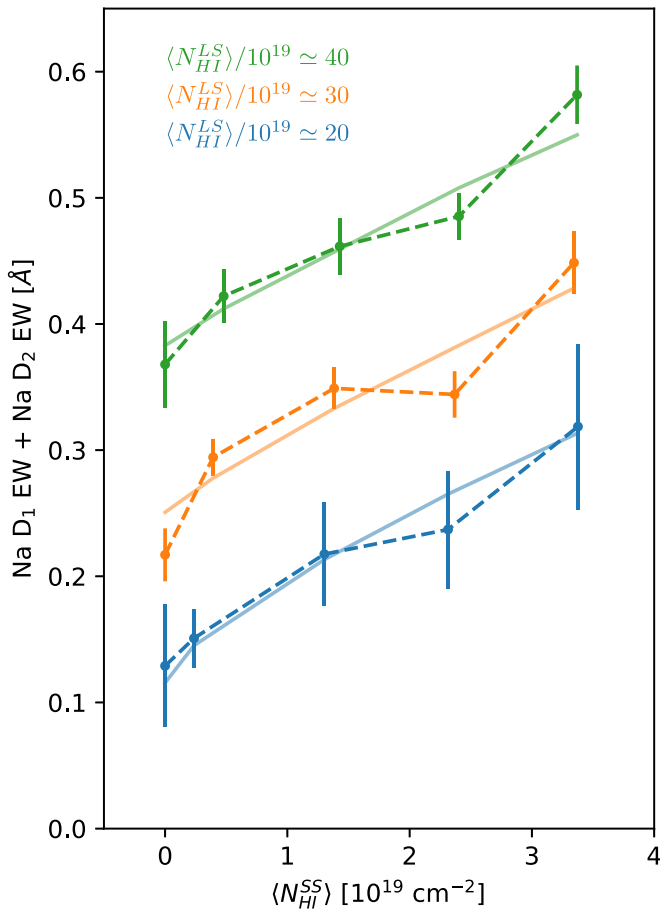
Figure 3. Integrated Na I D equivalent widths. Fits to Equation (3) are overplotted in solid lines. Bins are located on the abscissa by their median small-scale column, $\langle N_{\text{H I}}^{\text{SS}} \rangle$.

Figure 3. These data are then fit with a simple model,

$$\langle \text{EW}_{\text{Na I D}_1} \rangle + \langle \text{EW}_{\text{Na I D}_2} \rangle = C^{\text{LS}} \frac{\langle N_{\text{H I}}^{\text{LS}} \rangle}{10^{19} \text{ cm}^{-2}}$$
$$+ C^{\text{SS}} \frac{\langle N_{\text{H I}}^{\text{SS}} \rangle}{10^{19} \text{ cm}^{-2}} + \text{EW}_0, \qquad (3)$$

as shown in Figure 3. We find $C^{\text{SS}} = 41.5 \pm 6.1$ mÅ, $C^{\text{LS}} = 10.8 \pm 0.8$ mÅ, and $\text{EW}_0 = -50 \pm 27$ mÅ. This is to say that the total EW of Na I is nearly four times as sensitive to the column of small-scale H I structure than it is to that of large-scale structure

3.5. Variations

This analysis makes many specific choices, but the basic result, that C^{SS} is significantly larger than C^{LS}, is quite robust. The total EW of Na I is much more sensitive to the column density of small-scale structure than of large-scale structure. We find this same result if we switch to using means instead of medians, if we vary the bin edges and numbers, and if we use the total $N_{\text{H I}}$ as a proxy for $N_{\text{H I}}^{\text{LS}}$. We can even conduct the analysis without binning at all, and simply integrate over the Na I D$_1$ and Na I D$_2$ lines to find the total EW for each line of sight: we still find the same qualitative result. The procedure described in previous sections was selected because it allows for the easiest visual confirmation of our results, and follows

previous work with these data (Poznanski et al. 2012; Murga et al. 2015).

The Rolling Hough Transform (RHT; Clark et al. 2014) was designed to find linear features, whose properties in these same data were shown to be consistent with CNM. The RHT is a sequence of imaging processing steps, with the unsharp mask (USM) as the first step. Thus, it is not at all surprising that over the region we examine in this work 87% of the RHT-detected pixels overlap with the USM pixels described in Section 3.1. (RHT-detected pixels are simply the pixels with nonzero RHT intensity as described in Clark et al. 2014 for the data in Section 3.1, plus weak thresholding to suppress imaging artifacts.) Indeed, we see the expected trend when we examine pixels highlighted by the RHT: controlling for total H I column, these magnetically aligned structures are higher in Na I D EW.

4. Discussion

This analysis shows that the EW of interstellar Na I D$_1$ and Na I D$_2$ absorption is almost four times more strongly dependent on the column density of small-scale structure in neutral hydrogen, $N_{\text{H I}}^{\text{SS}}$, than it is on the column density of larger-scale structure $N_{\text{H I}}^{\text{LS}}$ or the overall column $N_{\text{H I}}$. This is quite consistent with a picture in which this small-scale structure represents the cooler, denser part of the ISM, as we have suggested previously (Clark et al. 2014, 2019). Na I / $N_{\text{H I}}$ will increase in denser regions due to the n^2 scaling of recombination. Na I / $N_{\text{H I}}$ will also increase in cooler regions due to the $T^{-0.7}$ scaling of the radiative recombination coefficient (Draine 2011). This leads to a higher Na I column (as probed with the Na I D$_1$ and Na I D$_2$ lines) per unit $N_{\text{H I}}$ than the typical ISM, which produces the trend $C^{\text{SS}} > C^{\text{LS}}$.

In contrast, a velocity-crowding origin for the small H I structure would yield no trend or the opposite trend. If the state of the ISM is not related to the intensity of smaller structures in the neutral ISM, the trends between Na I D$_1$ and Na I D$_2$ EW and $N_{\text{H I}}$ should generically be independent of whether the $N_{\text{H I}}$ is in smaller structures or larger structures; $C^{\text{SS}} = C^{\text{LS}}$. Further, if small-scale structure is created by velocity crowding in the H I, Na I D absorbers should also have more crowding. We note that since Na I D lines are narrower than H I lines, the crowding will be less severe, but nonetheless, lines of sight with more H I crowding will have more Na I D crowding. This will naturally enhance the optical depth of the stronger saturated line, which will in turn drive down the measured EW per $N_{\text{H I}}$. Thus, a velocity-crowding origin predicts $C^{\text{SS}} = C^{\text{LS}}$ or $C^{\text{SS}} < C^{\text{LS}}$ if Na opacity effects are taken into account, both of which are inconsistent with our result.

5. Conclusion

We stacked 50,985 SDSS DR7 spectra at high Galactic latitude, binned against the smooth H I column density $N_{\text{H I}}^{\text{LS}}$ and small-scale structure column density in thin velocity channels, $N_{\text{H I}}^{\text{SS}}$, as measured by GALFA-H I DR2. We find the Na I D$_1$ and Na I D$_2$ EW measured in these median stacks are nearly four times as sensitive to $N_{\text{H I}}^{\text{SS}}$ as $N_{\text{H I}}^{\text{LS}}$. This is consistent with a picture in which small H I structure is dominated by cool, dense media, but inconsistent with a picture in which the small structure is velocity crowding.

There are two main upshots of this result. The first is conclusive proof that small structures in velocity slices of

21 cm measurements indeed have a significant overabundance of cooler, denser ISM. The exact composition of this material is still unknown, and we have not measured the relative balance of warm, unstable, cold, diffuse molecular, and dense molecular gas. A more precise measurement with higher spectral resolution and using a broader range of ions would be very illuminating in terms of the precise nature of the gas in question, perhaps using the KODIAQ archive (O'Meara et al. 2017), the Hubble Spectroscopic Legacy Archive (Peeples et al. 2017), and COS-GAL (Zheng et al. 2019).

The second upshot is that a number of statistical tools developed for the study of ISM turbulence and magnetization must be dramatically rethought. Many methods, e.g., Velocity Channel Analysis (VCA; Lazarian & Pogosyan 2000), rely on the notion that small-scale structures are driven by velocity-crowding effects. While it is certain that the details of which structures appear at which velocities will be affected by the divergence and convergence of the velocity field along the line of sight, it is clearly unacceptable to use statistical tools that entirely ignore the fact that these structures are preferentially cool, dense media. The high-wavenumber end of the narrow-channel H I spatial power spectrum probes the density distribution of cold gas. The relative prominence of cold gas in narrower velocity channels will flatten the slope of the spatial power spectrum, creating the effect some have attributed to the velocity field. Thus, tools like VCA will need to be overhauled before they can be reliably used to measure physical properties of the ISM.

ORCID iDs

J. E. G. Peek ⓘ https://orcid.org/0000-0003-4797-7030
S. E. Clark ⓘ https://orcid.org/0000-0002-7633-3376

References

Abazajian, K. N., Adelman-McCarthy, J. K., Agüeros, M. A., et al. 2009, ApJS, 182, 543
Astropy Collaboration, Price-Whelan, A. M., Sipőcz, B. M., et al. 2018, AJ, 156, 123
Astropy Collaboration, Robitaille, T. P., Tollerud, E. J., et al. 2013, A&A, 558, A33
Blagrave, K., Martin, P. G., Joncas, G., et al. 2017, ApJ, 834, 126
Clark, S. E. 2018, ApJL, 857, L10
Clark, S. E., Hill, J. C., Peek, J. E. G., Putman, M. E., & Babler, B. L. 2015, PhRvL, 115, 241302
Clark, S. E., Peek, J. E. G., & Miville-Deschênes, M.-A. 2019, ApJ, 874, 171
Clark, S. E., Peek, J. E. G., & Putman, M. E. 2014, ApJ, 789, 82
Cox, D. P. 2005, ARA&A, 43, 337
Draine, B. T. 2011, Physics of the Interstellar and Intergalactic Medium (Princeton, NJ: Princeton Univ. Press)
Hobbs, L. M. 1975, ApJ, 202, 628
Hunter, J. D. 2007, CSE, 9, 90
Jelić, V., de Bruyn, A. G., Pandey, V. N., et al. 2015, A&A, 583, A137
Kalberla, P. M. W., & Haud, U. 2019, A&A, 627, A112
Kalberla, P. M. W., & Kerp, J. 2009, ARA&A, 47, 27
Kalberla, P. M. W., Kerp, J., Haud, U., et al. 2016, ApJ, 821, 117
Lazarian, A., & Pogosyan, D. 2000, ApJ, 537, 720
Lazarian, A., & Yuen, K. H. 2018, ApJ, 853, 96
Martin, P. G., Blagrave, K. P. M., Goncalves, D. P., et al. 2015, ApJ, 809, 153
McClure-Griffiths, N. M., Dickey, J. M., Gaensler, B. M., Green, A. J., & Haverkorn, M. 2006, ApJ, 652, 1339
Murga, M., Zhu, G., Ménard, B., & Lan, T.-W. 2015, MNRAS, 452, 511
Murray, C. E., Peek, J. E. G., Lee, M.-Y., & Stanimirović, S. 2018, ApJ, 862, 131
Oliphant, T. E. 2015, Guide to NumPy (2nd ed.; USA: CreateSpace Independent Publishing Platform)
O'Meara, J. M., Lehner, N., Howk, J. C., et al. 2017, AJ, 154, 114
Peek, J. E. G., Babler, B. L., zheng, Y., et al. 2018, ApJS, 234, 2
Peek, J. E. G., Heiles, C., Douglas, K. A., et al. 2011, ApJS, 194, 20
Peeples, M., Tumlinson, J., Fox, A., et al. 2017, Instrument Science Rep. COS 2017-4
Planck Collaboration, Adam, R., Ade, P. A. R., et al. 2016, A&A, 586, A135
Poznanski, D., Prochaska, J. X., & Bloom, J. S. 2012, MNRAS, 426, 1465
Prochaska, J. X. 2017, A&C, 19, 27
Spitzer, L. 1978, Physical Processes in the Interstellar Medium
Zheng, Y., Peek, J. E. G., Putman, M. E., & Werk, J. K. 2019, ApJ, 871, 35
Zhu, G., Ménard, B., Bizyaev, D., et al. 2014, MNRAS, 439, 3139